

SMT-EX: An Explainable Surrogate Modeling Toolbox for Mixed-Variables Design Exploration

Mohammad Daffa Robani
AwanTunai, Urban Suites, 3 Hullet Road, Singapore, 229158

Paul Saves*
DTIS, ONERA, Université de Toulouse, 31000 Toulouse, France
Fédération ENAC ISAE-SUPAERO ONERA, Université de Toulouse, 31000 Toulouse, France

Lavi Rizki Zuhalf†, Pramudita Satria Palar‡
Bandung Institute of Technology, Bandung, Indonesia, 40132

Joseph Morlier§
ICA, Université de Toulouse, ISAE-SUPAERO, MINES ALBI, UPS, INSA, CNRS, 3 rue Caroline Aigle, Toulouse, 31400, France

Surrogate models are of high interest for many engineering applications, serving as cheap-to-evaluate time-efficient approximations of black-box functions to help engineers and practitioners make decisions and understand complex systems. As such, the need for explainability methods is rising and many studies have been performed to facilitate knowledge discovery from surrogate models. To respond to these enquiries, this paper introduces SMT-EX, an enhancement of the open-source Python Surrogate Modeling Toolbox (SMT) that integrates explainability techniques into a state-of-the-art surrogate modelling framework. More precisely, SMT-EX includes three key explainability methods: Shapley Additive Explanations, Partial Dependence Plot, and Individual Conditional Expectations. A peculiar explainability dependency of SMT has been developed for such purpose that can be easily activated once the surrogate model is built, offering a user-friendly and efficient tool for swift insight extraction. The effectiveness of SMT-EX is showcased through two test cases. The first case is a 10-variable wing weight problem with purely continuous variables and the second one is a 3-variable mixed-categorical cantilever beam bending problem. Relying on SMT-EX analyses for these problems, we demonstrate its versatility in addressing a diverse range of problem characteristics. SMT-Explainability is freely available on Github*.

I. Introduction

Numerous engineering tasks, including optimization, sensitivity analysis, and uncertainty quantification, often require multi-query calls that involve repeated use of computationally intensive solvers, such as high-fidelity computational fluid dynamics [1]. Surrogate models are commonly employed to efficiently address multi-query tasks [2]. These models serve as cost-effective approximations of black-box functions, constructed using a limited number of data points. The data is usually obtained from computer simulations (such as computational fluid dynamics or finite element simulations) or physical experiments. Essentially, it consists of pairs of data points and their corresponding responses. Some popular types of surrogate models in engineering literature include Gaussian Process Regression (GPR) [3], polynomial chaos expansion [4] and neural networks [5]. The importance of the surrogate model in the modern engineering landscape cannot be overstated since it provides means to significantly reduce the turn-around time for more efficient optimization [6, 7], design exploration, and sensitivity analysis [8], among others.

Several open-source surrogate modeling tools have been developed to assist engineers in implementing surrogate models. In particular, the Surrogate Modeling Toolbox (SMT) [9, 10] is an open-source framework offering functions

*Ph.D, email: paul.saves@onera.fr

†Professor, Faculty of Mechanical and Aerospace Engineering, lavirz@ae.itb.ac.id

‡Assistant Professor, Faculty of Mechanical and Aerospace Engineering, pramsp@itb.ac.id (Corresponding author)

§Professor, email: joseph.morlier@isae-supaero.fr

*<https://github.com/SMTorg/smt-explainability>

to efficiently construct surrogate models. An important key surrogate model implemented in SMT is the GPR, also known as the Kriging model. The latter is a probabilistic framework for approximating a black-box function that can predict both a mean value prediction and an uncertainty quantification and can therefore be used for Monte Carlo computations [11] and variance-based sensitivity analysis [12]. The versatility of GPR has proven useful for various enhancements that improve its ability to address different types of problems. To handle various input types, SMT has extended GPR to accommodate mixed-integer and mixed-categorical variables [13]. As a surrogate modeling tool, various experiments have shown that the GPR module of SMT has better predictive power than other similar tools, *e.g.*, UQlab [14] and scikit-learn for a fixed number of points [15]. Thus, SMT shows promise for various real-world applications and has the potential to expand its capabilities further. This paper focuses on the extension of SMT to expand its capabilities beyond as a data-driven prediction tool. Specifically, this work enhances SMT functionalities by adding a knowledge discovery tool, which will be explained shortly.

Engineers frequently aim to derive meaningful insights from constructed surrogate models. For example, understanding the influence of input variables on the output can facilitate the reduction of the problem’s dimensionality. Additionally, engineers often seek to determine the complexity of the input-output relationship, such as the degree of nonlinearity. These tasks are more easily accomplished when the problem exhibits low dimensionality in terms of input variables but it is not a trivial task to gain such an understanding for problems with high-dimensional input [16]. High accuracy is often gained by sacrificing the interpretability of the model, which makes knowledge extraction even more difficult. Additional efforts are then necessary to be able to gain understanding. To that end, explainability serves as a powerful means to “dissect” the input-output relationship and provide knowledge to the user [17–19]. The term explainability itself originated from the machine learning community, which aims to improve the transparency of the model and eventually enhance our trust in the model. However, in this paper, we particularly focus on the role of explainability in knowledge extraction and scientific understanding. Several explainability methods have been proposed, including SHapley Additive Explanations (SHAP) [20], Accumulated Local Effects (ALE) [21], Partial Dependence Plots (PDP) [22], and Individual Conditional Expectations (ICE) [23]. Each method reveals understanding from various viewpoints, which is why it is essential to deploy various methods when dealing with a single problem. While explainability originated in the machine learning and statistics community, methods from other fields, like Global Sensitivity Analysis (GSA) [24] and active subspace [25], also strive to offer insights into the constructed model. In particular, variance-based GSA methods like Sobol’ indices aim to rank the significance of input variables based on specific rules, using variance decomposition as their foundation [26]. An in-depth literature on the subject can be found here [27]. Conversely, active subspace enables the identification and visualization of low-dimensional latent spaces within the input-output relationship. In the field of engineering design, the authors have made several contributions, including the analytical calculation of SHAP for PCE [28] and the development of a multi-objective design exploration method using SHAP [29]. We have also successfully applied explainability to various engineering design problems, such as for distributed electric propulsion aircraft design [30].

In this paper, we present an extension of the SMT toolbox, named SMT-EX, which is specifically designed for explainability analysis. Our primary aim is to provide users with an easy-to-use explainability tool that can be readily deployed once the surrogate model has been constructed with SMT. The SMT-EX features several explainability submodules, including SHAP, PDP, ICE, and Sobol’ indices. Thanks to the original capabilities of the SMT, the developed explainability module is also equipped with the ability to provide explainability for both continuous and mixed-categorical variables. Besides, we have implemented the module for uncertainty quantification using conformal prediction in SMT. The uncertainty quantification subroutine itself can be seen as a part of “explainability” since it provides a means to make the model transparent. It is based on a simple split prediction from [31].

In this paper, we demonstrate the applicability of SMT-EX for two test problems with various characteristics, namely, a 10-variable wing weight problem with all continuous variables and a 3-variable mixed-categorical cantilever beam problem.

II. SMT 2.0: Surrogate Modeling Toolbox

Let us denote the vector of input variable $\mathbf{x} = [x_1, x_2, \dots, x_m]^T$, where m is the size of input variables. The aim is to approximate a black-box function $f(\mathbf{x})$ with a surrogate model $\hat{f}(\mathbf{x})$, where

$$f : \Omega \times \mathbb{F}^l \rightarrow \mathbb{R}, \quad (1)$$

$\Omega \subset \mathbb{R}^{m_c}$ is the continuous design set for m_c continuous variables, and $\mathbb{F}^l = \{1, \dots, L_1\} \times \{1, \dots, L_2\} \times \dots \times \{1, \dots, L_l\}$ is the input space for l categorical variables with L_1, \dots, L_l represent their respective levels.

SMT 2.0 is a Python package offering a comprehensive suite of surrogate modeling techniques[†], sampling strategies, and benchmarking tools. SMT features an intuitive library of surrogate models and facilitates the incorporation of new methods with ease. It is the product of collaborative efforts between various institutions, including ONERA, NASA Glenn, ISAE-SUPAERO/ICA, University of Michigan, Polytechnique Montréal, and the University of California San Diego. Several unique modules and capabilities of SMT include gradient-enhanced modeling and unique surrogate models (*e.g.*, Kriging with partial least squares [32] and energy-minimizing spline interpolation [33]). The newest SMT version is SMT 2.0, with additional modules focusing on hierarchical and mixed-variables Gaussian processes. This toolbox is open-source, and, as such, can be used for optimization and understanding with other software such as SBArchOpt [34] or SEGOMOE [35] but these applications were limited to simple Monte Carlo and Bayesian optimization and need to be extended for explainability, especially when dealing with architecture problems, *e.g.*, as discussed in [30].

In this paper, with an emphasis on explainability, we focus on the GPR implemented in SMT. The strength of GPs lies in their ability to handle small to medium-sized data sets, typical of engineering problems that involve computationally expensive simulations during data generation. Moreover, SMT surrogate models module accommodates various types of input variables, including its latest capability to address mixed-categorical problems, which is pertinent to one of the problems discussed in this paper. It is worth noting that the explainability module in SMT-EX is versatile and can be integrated with any type of surrogate model in SMT, not just limited to GPR.

SMT has been used in various engineering applications, and it will be beneficial for the users to enhance its capability with an additional tool that can help users understand their models, as explained in the next section. However, SMT has heavily focused on GPR models and derivative predictions for application in surrogate-based modelling or optimization. As such, for a given point, we can, not only predict the value at this point but put this prediction within a context and quantify uncertainty among others. More details are given hereinafter.

A. Gaussian process predictions

GPR are a powerful tool in surrogate modelling, especially for their ability to quantify uncertainty in predictions. A Gaussian Process (GP) provides a probabilistic model that represents the output as a collection of random variables with a joint Gaussian distribution. This approach enables the estimation of both mean predictions and variance for each input, effectively providing a natural mechanism for uncertainty quantification.

Given a set of observations $\mathcal{D} = \{(\mathbf{x}_i, y_i)\}_{i=1}^n$ where $y_i = f(\mathbf{x}_i) + \epsilon_i$ (with ϵ_i being Gaussian noise), the GP prior for the function f is specified by a mean function $m(\mathbf{x})$ and a covariance function $k(\mathbf{x}, \mathbf{x}')$. For most practical applications, we often assume a zero mean function, simplifying our focus to the covariance structure. The prediction at a new point \mathbf{x}_* can be expressed as:

$$\hat{y}_* = m(\mathbf{x}_*) + k(\mathbf{x}_*, \mathbf{X})^T K^{-1}(\mathbf{y} - m(\mathbf{X})), \quad (2)$$

$$\sigma_*^2 = k(\mathbf{x}_*, \mathbf{x}_*) - k(\mathbf{x}_*, \mathbf{X})^T K^{-1} k(\mathbf{x}_*, \mathbf{X}), \quad (3)$$

where K is the covariance matrix computed from the training data, and $k(\mathbf{x}_*, \mathbf{X})$ represents the covariance between the new point and the training points. In particular, in the mixed categorical setting, this matrix depends on some other matrices of correlation between the levels of every categorical variables [13]. This matrices are used internally by the GP and automatically learn and as such, we propose to display them as they reflect the learned correlations between the levels of the inputs categorical variables [16]. In a more supervised context, by coupling with a clustering algorithm, one can impose a structure on the learned correlation hyperparameters to infer more easily "group of levels" that behave the same [36].

The confidence interval can be derived from the predictive distribution of y_* , which is Gaussian with mean \hat{y}_* and variance σ_*^2 . A $100(1 - \alpha)\%$ confidence interval for a new observation y_* can then be expressed as:

$$\hat{y}_* \pm z_{\alpha/2} \sigma_*, \quad (4)$$

where $z_{\alpha/2}$ is the critical value from the standard normal distribution corresponding to the desired confidence level. This interval provides a range of plausible values for the prediction, incorporating both the uncertainty in the model and the inherent noise in the observations. GPs and their ability to generate confidence intervals have found applications in various fields, including engineering optimization and machine learning. Notably, the integration of GPs with other methods, such as conformal prediction, enhances their reliability and applicability in decision-making processes [37].

[†]The SMT explainability module is part of the SMTorg organization: <https://github.com/SMTorg>

B. Split conformal predictions

Conformal prediction is a powerful framework for quantifying the uncertainty of predictions made by machine learning models. Unlike traditional confidence intervals, conformal prediction enables adaptive and valid uncertainty quantification based on the specific data at hand. Split conformal prediction, in particular, enhances this framework by leveraging a calibration dataset to derive confidence intervals [38].

The general approach of split conformal involves splitting the available dataset \mathcal{D} into two parts: a training set $\mathcal{D}_{\text{train}} = \{(\mathbf{x}_i, y_i)\}_{i=1}^{n_{\text{train}}}$ for model fitting and a calibration set $\mathcal{D}_{\text{cal}} = \{(\mathbf{x}_j, y_j)\}_{j=1}^{n_{\text{cal}}}$ for assessing the model's predictive performance. Given a fitted model, we obtain predictions on the calibration data. Let \hat{y}_j be the predicted value for observation j in the calibration set. The residuals, defined as $r_j = |y_j - \hat{y}_j|$, reflect the differences between the observed and predicted values. These residuals help assess model prediction error, which indirectly reflects uncertainty [31].

To establish a confidence interval for a new observation \mathbf{x}_* , we first calculate the quantiles of the residuals. Specifically, we compute the $(1 - \alpha)$ quantile of the residuals from the calibration set, denoted as q_α , where α represents the significance level. This can be mathematically represented as:

$$q_\alpha = \text{Quantile}_{1-\alpha}(r_1, r_2, \dots, r_{n_{\text{cal}}}),$$

where r_j are the computed residuals from the calibration set. Finally, the confidence interval for a new observation \mathbf{x}_* can be expressed as:

$$\hat{y}_* \pm q_\alpha,$$

where \hat{y}_* is the prediction made by the model for \mathbf{x}_* . This confidence interval guarantees valid coverage probability under the assumption that the calibration set is representative of the underlying distribution of the data.

Theoretical guarantees for conformal prediction stem from the notion of exchangeability, which ensures that the predictions made on unseen data are valid, meaning they will cover the true values with the desired probability $1 - \alpha$ [39]. This confidence interval guarantees valid coverage probability under the assumption that the calibration set is representative of the underlying distribution of the data. In the following, we will consider $\alpha = 10\%$, 80% of the data to train the model and the rest 20% for model calibration.

SMT does not come with tools to analyze and explain the dependency between variables and outputs, only the previously mentioned basic uncertainty quantification tools, therefore motivating for dedicated tools.

III. Explainability module for SMT-EX

SMT-EX incorporates three methods: SHAP, PDP, and ICE. These methods were deliberately chosen due to their widespread use in various machine-learning applications. They are well-suited to our objective of providing insight and knowledge to SMT users who build surrogate models for solving diverse engineering problems. The SMT-EX itself can be used with any type of surrogate model provided by SMT since the only required information is the prediction information. However, for demonstration purposes, we focus on the GPR from SMT since it can also handle mixed-categorical modelling. In addition, SMT-EX also implements Sobol' indices for problems with all continuous variables.

SHAP assigns each feature an importance value for a particular prediction, offering a comprehensive view of feature impact by considering all possible feature combinations. PDP illustrates the relationship between a feature and the predicted outcome by showing the average effect of a feature while averaging out the influence of other features. Finally, ICE plots provide a detailed view by showing how the prediction changes for individual instances as a particular feature varies, highlighting interactions and heterogeneities in feature effects. This section briefly explains these three methods and Sobol' indices.

In the following explanations, we will use the following notations. First, let $[1 : m] := \{1, \dots, m\}$ and $U \subseteq [1 : m]$ and $C := [1 : m] \setminus U$ as the complement of U . Further, let $\mathbf{x}_U := \{x_j : j \in U\}$ denote the vector of the input of interest and $\mathbf{x}_C := \{x_j : j \in C\}$ be the set of the other output. Let $|\cdot|$ be the cardinality of a set, we are primarily interested in cases with $|U| = 1$ or $|U| = 2$ when performing visualization or GSA.

A. Sobol' indices

Sobol' decomposition works according to the following decomposition

$$f(\mathbf{x}) = f_\emptyset + \sum_{i=1}^m f_i(x_i) + \sum_{1 \leq i < j \leq m} f_{i,j}(x_i, x_j) + \dots + f_{1,2,\dots,m}(x_1, x_2, \dots, x_m) \quad (5)$$

where f_0 is defined such that

$$f_0 = \mathbb{E}[f(\mathbf{x})], \quad (6)$$

where $\mathbb{E}[\cdot]$ is the expectation operator. In this regard, f_i is the main effect of variable x_i and higher cardinality indicates interaction, *e.g.*, $f_{i,j}$ denotes the interaction effect between x_i and x_j . Each $f_U(\mathbf{x}_U)$ term but f_0 satisfies the following property:

$$\mathbb{E}[f_U(\mathbf{x}_U)|x_k] = 0 \quad \text{for any } k \in S. \quad (7)$$

The Sobol' indices quantify the contribution of each subset U to the total variance of $f(\mathbf{x})$. The total variance is defined as

$$\text{Var}[f(\mathbf{x})] = \sum_{\emptyset \neq U \subseteq [1:m]} \text{Var}[f_U(\mathbf{x}_U)] \quad (8)$$

where $\text{Var}[f_U(\mathbf{x}_U)]$ denotes the partial variance correspond to the subset U . We then have the following definitions of Sobol' indices:

$$S_U = \frac{\text{Var}[f_U(\mathbf{x}_U)]}{\text{Var}[f(\mathbf{x})]}. \quad (9)$$

For example, S_1 denotes the main effect of variable x_1 , $S_{1,2}$ denotes the interaction effect due to x_1 and x_2 .

A related metric is the total Sobol' index which represents the proportion of the output variance that can be attributed to the input variable, including all of its interactions with other variables. The total Sobol' index for the i -th variable is defined as

$$S_{T_i} = \sum_{\substack{U \subseteq [1:m] \\ i \in U}} S_U. \quad (10)$$

For example, if $m = 3$ then S_{T_1} is defined as $S_{T_1} = S_1 + S_{1,2} + S_{1,3} + S_{1,2,3}$ [26].

A Monte Carlo simulation can be used to estimate Sobol' indices for a given $f(\mathbf{x})$ and the range of \mathbf{x} [40]. It is worth noting that Sobol' indices are only valid in their general formulation for continuous (or at least ordered) variables because they rely on smoothly decomposing output variance across an infinite range of input values [41]. Furthermore, Sobol' indices provide only the importance of input variables and do not reveal the specific ways an input variable influences the output. This limitation necessitates the use of explainability methods like PDP, ICE, and SHAP, which become the core of the current SMT-EX version.

B. Partial Dependence Plots and Individual Conditional Expectations

The partial dependence function [22] can be expressed as

$$f_{pd}(x_U) = \mathbb{E}_{\mathbf{x}_C} [\hat{f}(\mathbf{x}_U, \mathbf{x}_C)] = \int f(\mathbf{x}_U, \mathbf{x}_C) dP(\mathbf{x}_C) \approx \frac{1}{n_r} \sum_{i=1}^{n_r} f(\mathbf{x}_U, \mathbf{x}_C^{(i)}), \quad (11)$$

where n_r is the size of points for the estimation of PDP. Creating a plot of the partial dependence function illustrates how the subset of input variables (*i.e.*, \mathbf{x}_U) affects the model's predictions while accounting for the influence of other features (*i.e.*, \mathbf{x}_C) through marginalization or averaging. Observing the average predictions at varying values of the chosen feature allows us to detect patterns and trends, making the model easier to interpret and aiding informed decision-making. To put it simply, PDP shows the overall trend observed when a specific input changes, helping to identify trends like nonlinearity (in an average sense). However, since PDP reflects an average impact, some details might be obscured due to this aggregation. For example, PDP does not visualize possible interactions due to the interaction between \mathbf{x}_S and the other variable.

ICE plots extend PDPs by showing the effect of an input variable on predictions at the individual observation level [23]. Instead of averaging over all data points, an ICE plot provides a line for each instance, revealing how changing an input value affects that specific observation. In consequence, an ICE curve is essentially $\hat{f}(x_U, \mathbf{x}_C^{(i)})$ as in Eq. (11) for a sample $\mathbf{x}^{(i)}$. It is worth noting that PDP itself is essentially an aggregation of ICE curves. By averaging the individual effects, PDP provides a more general view of how an input variable impacts prediction. ICE plots, on the other hand, help identify interactions or non-linear relationships by showing the variation in how different observations respond to changes in a particular input. In practice, both PDP and multiple ICE curves are often depicted together, so that the trend can be seen from both global and more granular viewpoints.

One useful feature of PDP is the feature importance derived from the Partial Dependence (PD) function [42]. In this regard, feature importance from PDP calculates the standard deviation of the partial dependence function, reflecting

the variability and influence of a specific feature on the model's predictions. Let us denote the corresponding feature importance for the j -th variable as $I_{PD}(x_j)$ (i.e., $|U| = 1$):

$$I_{PD}(x_j) = \sqrt{\frac{1}{n_{PD} - 1} \sum_{i=1}^{n_{PD}} (f_{pd}(x_j^{(i)}) - \frac{1}{n_{PD}} \sum_{i=1}^{n_{PD}} f_{pd}(x_j^{(i)}))^2}, \quad (12)$$

where n_{PD} is the number of samples tried for calculating I_{PD} . Unlike Sobol' indices, the PD feature importance also applies for categorical variables with some modifications. For categorical inputs, the feature importance is calculated as follows:

$$I_{PD}(x_j) = \left(\max_k \left(f_{pd} \left(x_s^{(k)} \right) \right) - \min_k \left(\hat{f}_S \left(x_s^{(k)} \right) \right) \right) / 4, \quad (13)$$

where k is the number of unique values for the categorical feature of interest.

C. Shapley Additive Explanations and Individual Conditional Expectations

For easier notations in the following explanations, let us denote $-U = [1 : m] \setminus U$. A Shapley value can be computed for each data point, indicating the importance of the associated feature in classifying that specific data point $\mathbf{x}^{(i)}$, which reads as follows:

$$\phi_j(\mathbf{x}^{(i)}) = \frac{1}{m} \sum_{U \subseteq -j} \binom{m-1}{|U|}^{-1} (\text{val}(U \cup j) - \text{val}(U)), \quad (14)$$

where $\text{val}(\cdot)$ denotes the value function, which is based on the model's prediction and measures the benefit gained from individual or multiple variables working together [43]. For example, $\text{val}(U) = \hat{f}(\mathbf{x}_U^{(i)})$, where $\mathbf{x}_U^{(i)}$ is the subset of $\mathbf{x}^{(i)}$ that takes only the variables involved in U . In practice, SHAP is computed using approximation algorithms such as KernelSHAP to accelerate the computation time [44] for high-dimensional input. In SMT-EX, both exact and KernelSHAP are implemented. To calculate SHAP values, a reference value must be defined. For continuous variables with a known domain, it is advisable to set the reference value at the center of the input domain. When categorical variables are involved, a single unique value from the categorical feature should be chosen as the reference.

SHAP values are inherently localized, applying to individual samples within the input space. However, engineers often seek to understand the global impact of a specific input variable on the QoI. By plotting SHAP values across multiple samples in the input space, engineers can gain insights into how a particular input variable influences the QoI in a broader sense. This SHAP dependence plot allows for the observation of interactions and nonlinearities, providing a clearer overall picture. One useful feature of SHAP is that it provides the means for global sensitivity analysis through the averaged SHAP values. The averaged SHAP value for the j -th variable ($|\phi_j|$), can be computed as follows:

$$|\phi_j| = \frac{1}{n_{sh}} \sum_{i=1}^{n_{sh}} |\phi_j(\mathbf{x}^{(i)})| \quad (15)$$

where n_{sh} is the number of samples used for the calculation of averaged SHAP values.

Both PDP/ICE and SHAP can be used for mixed-categorical problems, which makes them useful for general applications in which non-continuous variables are also present.

IV. Application to engineering problems

A. A continuous 10-variable problem: Wing weight function

The first engineering application studied here is the wing weight problem that involves an analytical function that represents a light aircraft wing [45]. The target output is the wing's weight. The formula for calculating the wing weight is as follows:

$$f(\mathbf{x}) = 0.036 S_w^{0.758} W_{fw}^{0.0035} \left(\frac{A}{\cos^2(\Delta)} \right)^{0.6} q^{0.006} \lambda^{0.04} \left(\frac{100t_c}{\cos(\Delta)} \right)^{-0.3} (N_z W_{dg})^{0.49} + S_w W_p. \quad (16)$$

Table 1 shows a nomenclature of the symbols used in Eq. (16), as well as a baseline set of values, roughly representative of a Cessna C172 Skyhawk aircraft and a somewhat arbitrarily chosen range for each variable [45]. The expression

shown in Eq. (16) is quite convoluted and involves trigonometric, power terms, and multiplication of multiple variables, which gives an impression of nonlinearity. Thus, although the model itself is transparent, it is not a useful interpretable expression. We then applied SHAP and PDP/ICE from the SMT-EX module to visualize the behaviour of the 10-variable wing weight problem.

Table 1 Variables used in the wing weight function.

Variables	Variable Name (unit)	[lower, upper bound]
S_w	Wing area (ft ²)	[150, 200]
W_{fw}	Weight of fuel in the wing (lb)	[220, 300]
A	Aspect ratio	[6, 10]
Δ	Quarter-chord sweep (degrees)	[-10, 10]
q	Dynamic pressure at cruise (lb/ft ²)	[16, 45]
λ	Taper ratio	[0.5, 1]
t_c	Airfoil thickness to chord ratio	[0.08, 0.18]
N_z	Ultimate load factor	[2.5, 6]
W_{dg}	Flight design gross weight (lb)	[1700, 2500]
W_p	Paint weight (lb/ft ²)	[0.025, 0.08]

A GPR with a squared exponential covariance function was used as a surrogate model for this problem. For this problem, 300 data points were initially generated from the true function, Eq.(16), where 80% of the data is used to train the model and the rest 20% for model evaluation. After confirming its decent predictive performance that yields RMSE=0.144 in the test data, we employ SMT-EX to gain an explanation of the model. The SHAP and PDP/ICE plots generated by SMT-EX are shown in Fig. 1. Essentially, PDPs show that the trends are monotonous to all variables but the quarter chord sweep of the wing that alters the weight in a quadratic fashion. Although this makes sense from an engineering viewpoint, it is not easy to quickly grasp this from looking at Eq. (16). In this regard, explainability provides a valuable tool for examining the impact of each input variable on the output. Another information that can be deduced from the PDPs is how each input variable associates with the output. In addition to the quadratic trend resulting from the quarter chord sweep, it is evident that increasing all variables except t_c generally leads to an increase in wing weight. This insight is particularly valuable in applications like optimization, where understanding how to adjust input variables to optimize the objective function is essential.

The deviation of ICE curves from the main PDP plot signifies interactions between the variable of interest and other variables. This means that, depending on the values of other variables, the trend shown by the ICE curve might change. Essentially, ICE curves represent one-dimensional slices of the predictive model. Take the effect of N_z as an example. It can be observed that the gradient of each ICE curve differs, indicating that the impact of the slope on N_z varies based on the values of other input variables. Next, let us now examine the quarter-chord sweep (Δ), which consistently exhibits a quadratic trend regardless of the values of the other inputs, although its relative impact varies. ICE curves are also valuable for capturing changes in the association between an input variable and the output (*e.g.*, a shift from positive to negative correlation), though this characteristic is not observed in the current problem.

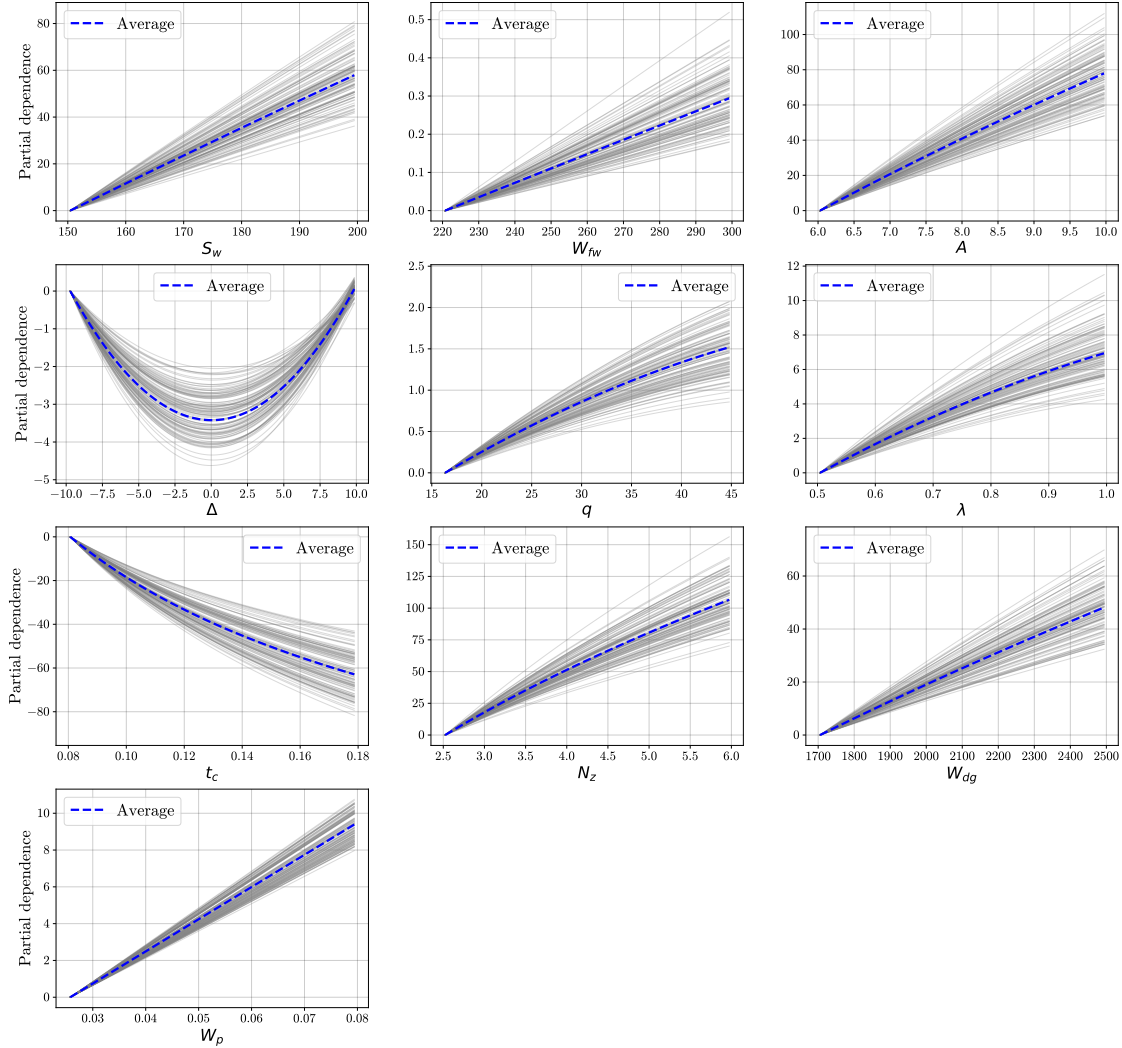


Fig. 1 Partial dependence plots and individual conditional expectations for the wing weight problem.

The SHAP dependence plots for the wing weight problem are presented in Fig. 2. Both plots (*i.e.*, SHAP and PDP/ICE) essentially convey similar information regarding the trend and magnitude of the impact. However, SHAP offers a different perspective on interactions compared to PDP and ICE. While PDP and ICE plots make it challenging to assess the strength of interactions, they provide a clearer view of the interaction dynamics. On the other hand, SHAP clearly demonstrates the presence of interactions, as indicated by the dispersion of SHAP values (if no interaction existed, there would be no dispersion). The interaction level is shown to be relatively weak here, as the dispersions are small, aligning with the expected intuition for the wing weight problem. Despite that, it is not easy to comprehend the impact of interactions on significantly less influential variables. For example, it is not easy to understand the interaction dynamics for q and W_{fw} . It is worth noting that visualization can also be shown by colouring the dots according to the magnitude of the other input variable.

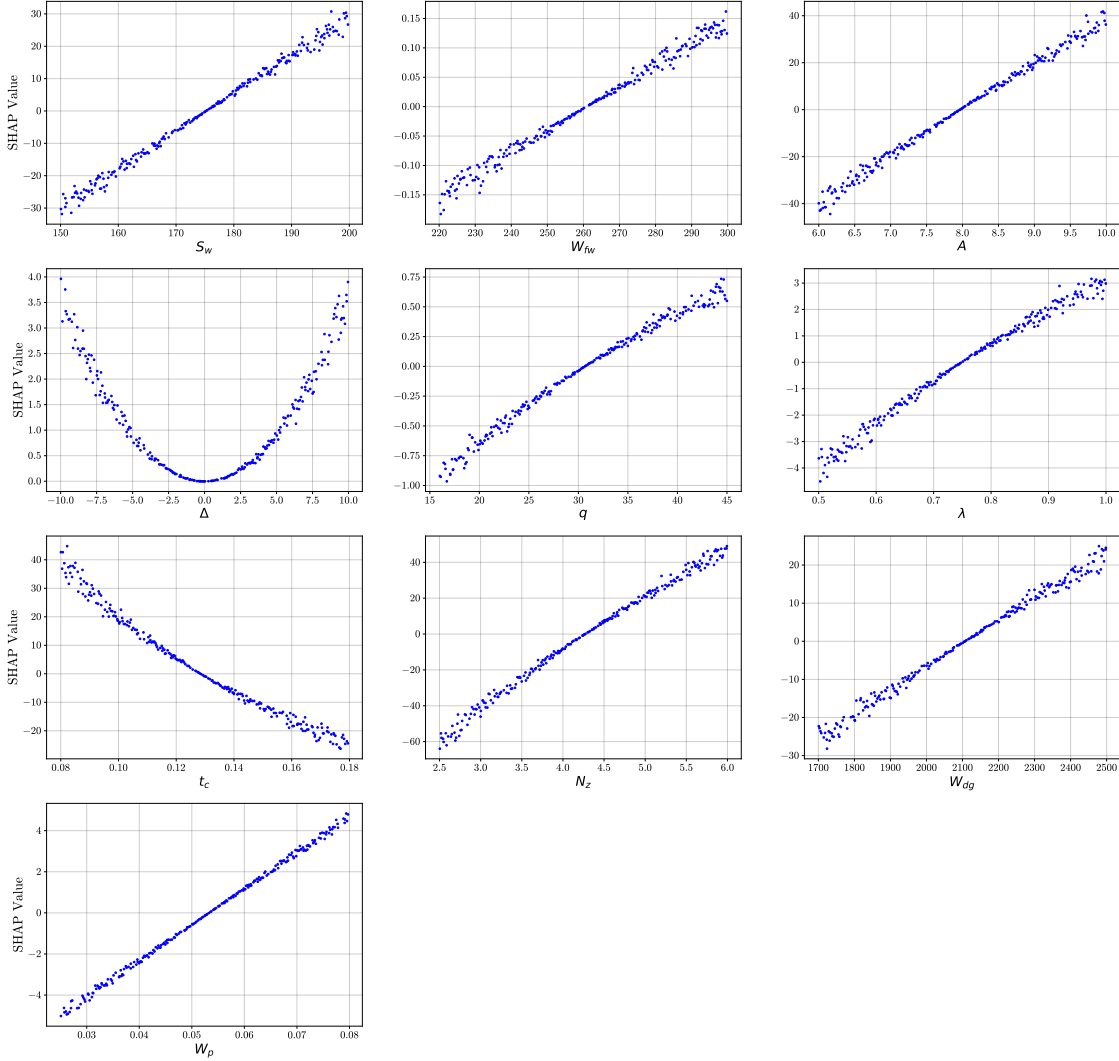


Fig. 2 SHAP dependence plots for the wing weight problem.

Finally, the input importance plots (*i.e.*, GSA) for the wing weight problems according to PDP and SHAP generated by SMT-EX are shown in Fig. 3. Besides, we also show the first and total order Sobol' indices in Fig. 4, a feature that is also implemented in SMT-EX. All feature importance metrics convey similar information, in which N_z is the most influential variable on the wing weight, followed by A and t_c . Interestingly, it can be seen that the magnitudes of the feature importance from PDP and SHAP are similar, despite the different principles used to measure the feature importance. The two methods also successfully detect that some variables are non-influential, *e.g.*, λ , and W_{fw} . The observation aligns with the results of Morris's method presented in our previous paper [46] and Sobol' indices. It is worth noting that the feature importance from PDP measures the standard deviation of the partial dependence function, indicating the variability and influence of specific input variables on the model's predictions, on average. On the other hand, the averaged SHAP quantifies the contribution of each feature to the model's predictions by averaging the absolute Shapley values of that feature across all samples. It is also important to note that the relative differences between the Sobol' indices of all features are noticeably larger compared to the feature importance values from PDP and SHAP. This is because Sobol' indices are derived from variance and are squared quantities, which amplifies the differences.

This demonstration highlights the capabilities of SMT-EX in explaining the complexity of problems involving continuous variables. It is important to emphasize that while Sobol' indices quantify feature importance, they do not reveal the internal workings of the black-box function. In contrast, SHAP and PDP/ICE provide insights into these dynamics. As a surrogate modeling tool, SMT stands out by offering not only feature importance and GSA but also a deeper understanding of how input variables influence the predictions- which is enabled thanks to the SMT-EX.

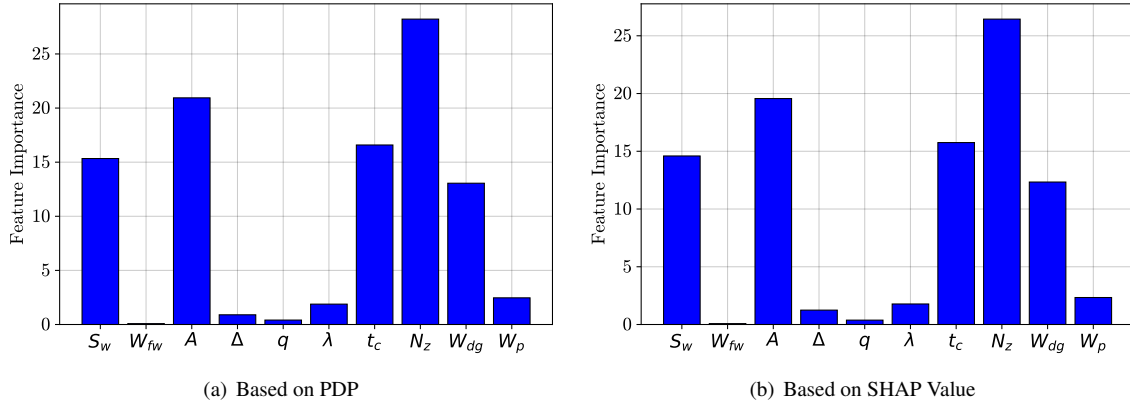


Fig. 3 Feature importance of the wing weight problem based on PDP and SHAP.

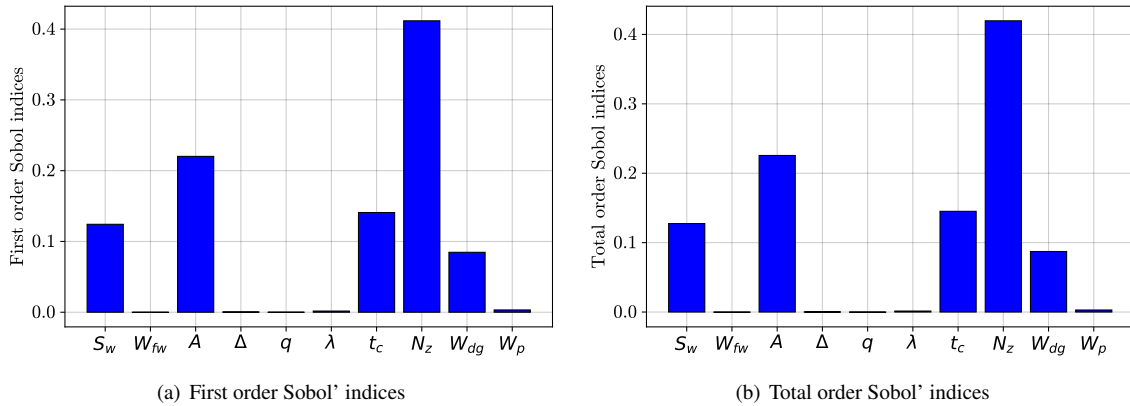


Fig. 4 First and total order Sobol' indices for the wing weight problem.

The confidence intervals are displayed in Fig. 5. Notice that a single GP was built with a single variable one at a time to provide insight into how conformal prediction performs compared to uncertainties from GP. To compute them, we use the same training and validation sets generated by LHS to cover the whole space. Using a surrogate model, such as a GP, we can see how moving along one variable affect the data dispersion on the remaining variables and quantify the dispersion. We can already make some comments on the results. Indeed, the conformal predictions are better than the confidence intervals as they are more adaptive to the position of a given point but here the uncertainty is not highly informative, the models are linear and the conformal intervals are similarly linear. The predicted uncertainty is also higher on the boundary of the domain which is a known effect for when the boundary lacks points. More importantly, the variables W_{fw} , Δ , q , λ and W_p seem to have almost no effect on the wing weight output, confirming the feature importance analysis and going in the same sense as the Sobol' indices interpretation. Obviously, the bigger the aircraft, the more its weight and therefore increasing wing area S_w or wing aspect ratio A increases the output. Similarly, the wing should be more massive when the load factor N_z and the design weight W_{dg} increase. To finish with, the more the thickness to chord ratio t_c , the less the wing weight, probably because high values correspond to low aspect ratio. Compared to the previous one, this analysis can quantify the effect of a variable on the output along the range (positive or negative effect/linearity,...). Moreover, it is consistent with the feature importance as the model for N_z explains more the variance and, as such, yields to the tighter confidence intervals.

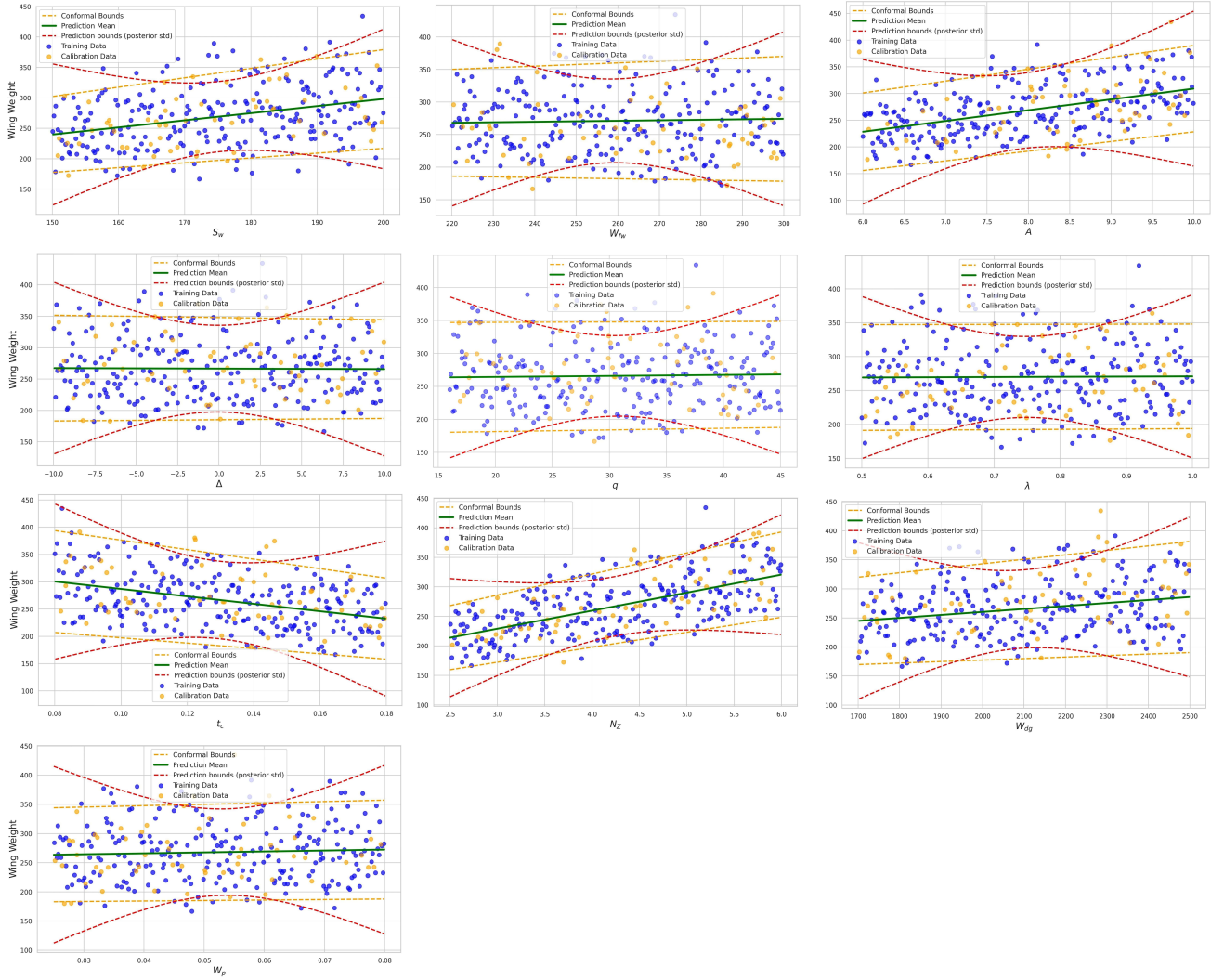


Fig. 5 Prediction intervals for the wing weight problem.

B. A mixed-categorical problem: Cantilever beam bending

The second engineering application is a beam bending problem in the linear elasticity range that features continuous and categorical variables, as shown in Fig. 6.

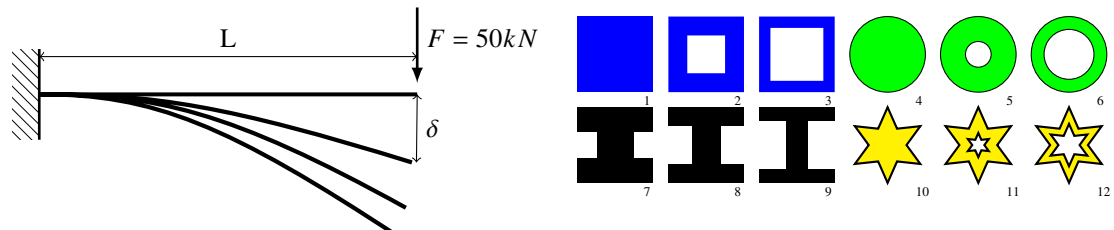


Fig. 6 Cantilever beam problem [13, Figure 6].

The beam is subjected to a force F applied to the free end. The Young modulus and the load were set to $E = 200$ GPa and $F = 50$ kN, respectively. The problem features two continuous variables, namely, the length $L \in [10, 20]$ (in m) and the surface $S \in [1, 2]$ (in m^2). Meanwhile, the categorical variable is the type of cross-section with 12 levels [36], each associated with the normalized moment of inertia \tilde{I} about the neutral axis. The values of the normalized

moment of inertia for each cross-section type are described in Table 2. For the square-shaped cross-section, B is more hollow than A, and C is more hollow than B. This pattern is consistent for the other shapes as well. The output of interest is the tip deflection at the free end, which reads as

$$\delta = f(L, S, \tilde{I}) = \frac{F L^3}{3E S^2 \tilde{I}}. \quad (17)$$

Table 2 Normalized moment of inertia for each type of cross-section.

Cross-section type	Normalized moment of inertia	Shape
A	0.0833	Square
B	0.139	Square
C	0.380	Square
D	0.0796	Circle
E	0.133	Circle
F	0.363	Circle
G	0.0859	I-beam
H	0.136	I-beam
I	0.360	I-beam
J	0.0922	Star
K	0.138	Star
L	0.369	Star

Therefore, a mixed-categorical GPR model $\hat{f}(L, S, \tilde{I})$ was built to approximate $f(L, S, \tilde{I})$. To the end, 300 data points are generated from the true function Eq. (17) where we used the same configuration of 80% samples as the training data and the remaining 20% for testing. The model obtained an RMSE of 10^{-4} in the test data, and we utilized SMT-EX again to extract the behaviour explanations learned by the model.

We first explored the application of conformal prediction for uncertainty quantification in this problem using the mixed-categorical GPR model $\hat{f}(L, S, \tilde{I})$. The boxplots illustrate the true values, the mean predictions from the Gaussian Process (GP), confidence intervals derived from conformal prediction ("conformal lower" and "conformal upper"), and confidence intervals obtained directly from GP ("prediction lower" and "prediction upper") at 300 new validation input points. A key observation here is that the lower bounds from conformal prediction align better with physical expectations compared to those from GP. Specifically, tip deflection should never be negative, as a negative prediction lacks physical validity. In this context, the lower bounds provided by conformal prediction are more reasonable, as they result in significantly fewer instances of negative tip deflection compared to GP.

To better understand the confidence intervals provided by conformal prediction, an additional set of GP models was constructed, each considering only one input variable at a time. For instance, a single GP model was developed using only L without considering S and the type of cross-section. The confidence intervals are displayed in Fig. 8. To compute them, we use the same training and validation sets generated by LHS to cover the whole space. Using a surrogate model, such as a GP, we can see how moving along one variable affects the data dispersion on the remaining variables and quantify the dispersion. We can already make some comments on the results. Indeed, the conformal predictions are better than the GP's confidence intervals as they are more adaptive to the position of a given point. More importantly, the lower bound is always between 0 and -0.0004 and always flat. Knowing that the true lower bound is a zero deflection because the response is strictly positive, conformal prediction is better to predict it on all three variables, especially for L where the lower bound is almost perfectly 0. Moreover, the conformal predictions indicate an increase in uncertainty when L increases and a decrease in uncertainty when S decreases. There is no significant effect of the cross-section shape on the uncertainty. However, more points lead to a decrease in standard deviation which explains why the traditional method underestimates the uncertainty on the cross-section G. Note that most data-centric methods depend highly on the data. For explainability, the initial distribution of points can significantly impact the results. When dealing with synthetic data, choosing the data sample may be a whole field of research to investigate [47].

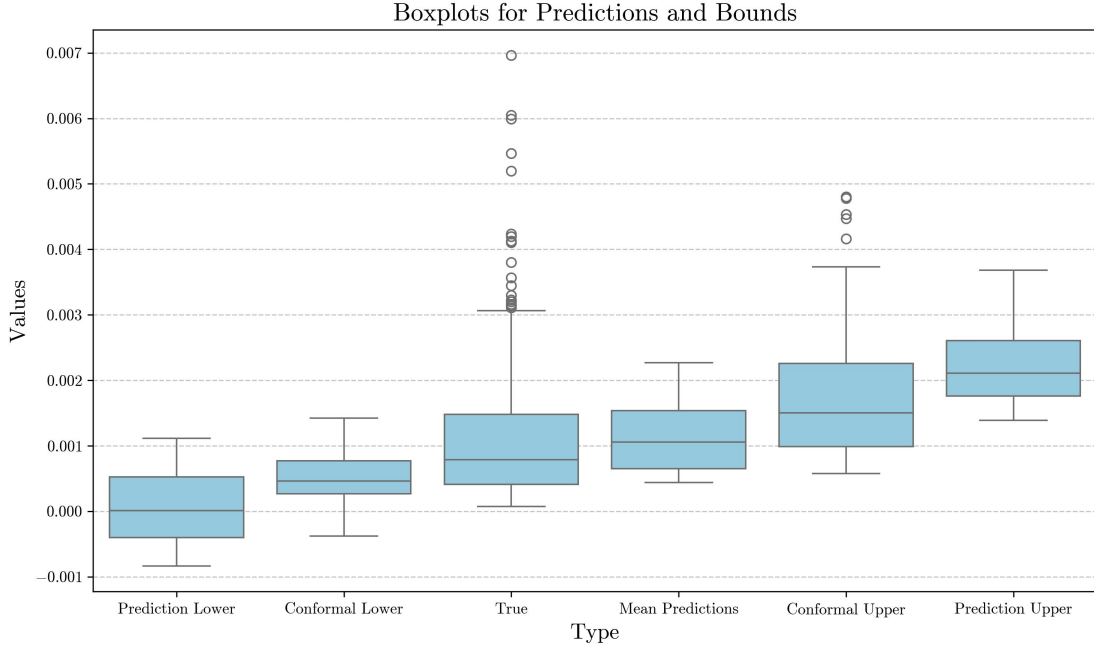


Fig. 7 Prediction intervals from the mixed-categorical GPR model $\hat{f}(L, S, \tilde{I})$ for the cantilever beam problem.

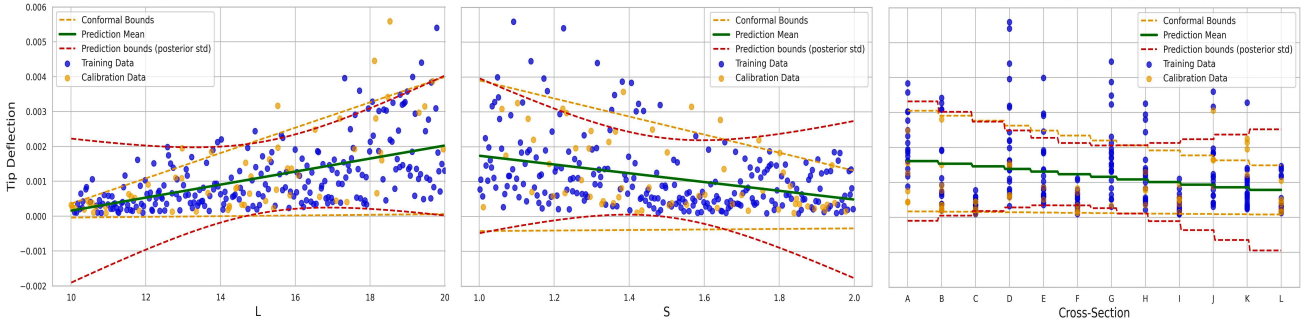


Fig. 8 Confidence interval for the cantilever beam problem.

Still using the GPR only, in Fig. 9, we have drawn the correlation matrix found between the cross-section shape (the resulting R_1 correlation matrix) for three categorical models: Gower distance, continuous relaxation and homoscedastic hypersphere [13]. On the figure below, the higher the correlation, the thinner the ellipse. As anticipated, the shapes are organized into three distinct groups based on their thickness levels: $\{1,4,7,10\}$, $\{2,5,8,11\}$, and $\{3,6,9,12\}$ meaning that the thickness of the cross-section matters more than its shape for predicting the tip deflection. Shapes within the same thickness group exhibit stronger correlations, indicating that thickness has a greater influence on tip deflection than cross-sectional shape. Additionally, in this dataset, any two points with similar values for L and S will yield similar outputs regardless of their cross-sectional design. This consistent influence of cross-section, modelled as $\frac{1}{L}$, results in high correlations when the likelihood is maximized. In Fig. 9c, using the EHH kernel, these three thickness groups can be clearly observed, with correlations nearing 1. Consequently, the homoscedastic hypersphere model [48] would produce a similar correlation matrix. Moreover, with the CR kernel shown in Fig. 9b, the middle-thickness group $\{2,5,8,11\}$ correlates with both the full and hollow groups, resulting in higher correlation values, whereas the correlation hyperparameters associated with the other two groups are smaller. In the GD model (Fig. 9a), only one primary positive correlation value is observed.

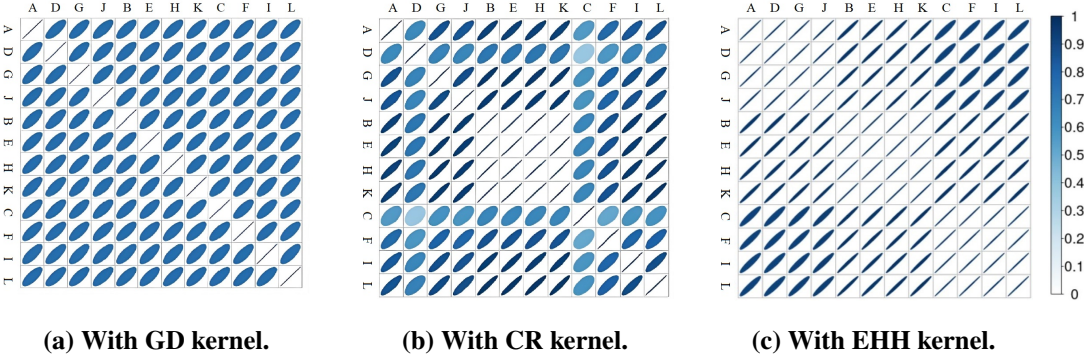


Fig. 9 Correlation matrix R_1^{cat} using different choices for Θ_1 for the categorical variable \tilde{I} from the cantilever beam problem.

By looking at the basic strength of the material equation (see Eq. (17)), it is clear that all variables interact with each other in how they affect the tip deflection. The PDP plots are shown in Fig. 10. Note that the plot for the categorical variable is shown in the form of a boxplot due to its non-continuous nature (with cross-section A serving as the reference). This means that the partial dependence of each category on the model’s predictions is represented by a boxplot, highlighting the distribution, central tendency, and variability of the model’s predictions for each category. For both length and surface area, the trends are clear and align with engineering principles: increasing the length leads to greater tip deflection, whereas increasing the surface area results in reduced tip deflection. Moreover, the presence of interactions is evident since the ICE curves deviate from the centred value (*i.e.*, partial dependence functions). For instance, the effect of increasing length on tip deflection depends on the type of cross-section and its area, as demonstrated by the variations in the ICE curves.

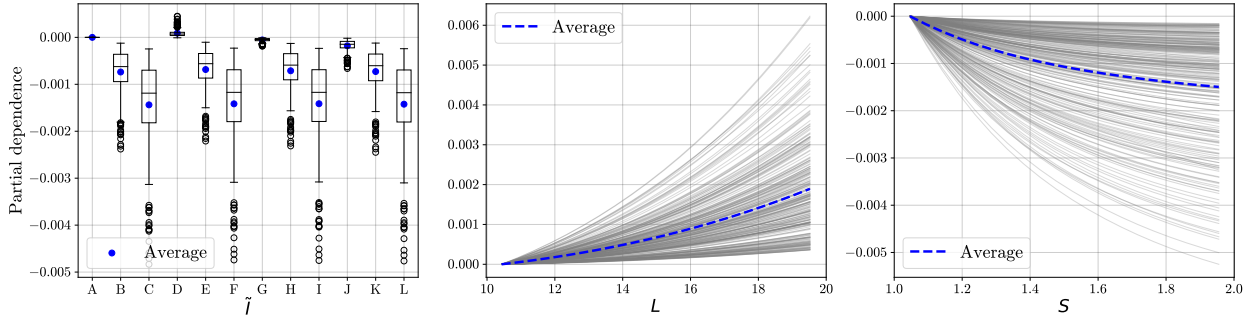


Fig. 10 Partial dependence plots and individual conditional expectations for the cantilever beam bending problem.

The PDP boxplot essentially shows the impact of the \tilde{I} , represented by various types of cross-sections. The result aligns with engineering principles, demonstrating that a more hollow cross-section (*e.g.*, C is more hollow than B and A) leads to reduced deflection due to the increased moment of inertia. Additionally, when comparing different sections with similar levels of hollowness (*e.g.*, C, F, I, and J), the impact on tip deflection is approximately the same. The relative change in impact is more significant when the level of hollowness varies because it greatly affects the moment of inertia. It is worth noting that this observation also aligns with the correlation matrix R_1^{cat} discussed earlier.

The SHAP dependence plots offer different viewpoints but still reveal similar insights illustrated in Figure 11. It is worth noting that the sign of the SHAP value only corresponds to the deviation from the mean or the centre. Thus, it is the trend that should be interpreted. The scattered SHAP values when plotted versus L and S indicated again the interactions between the three variables in affecting the tip deflection. The grouping of the unique values of \tilde{I} , representing the normalized moment of inertia, is also clearly observable from the SHAP dependence plots.

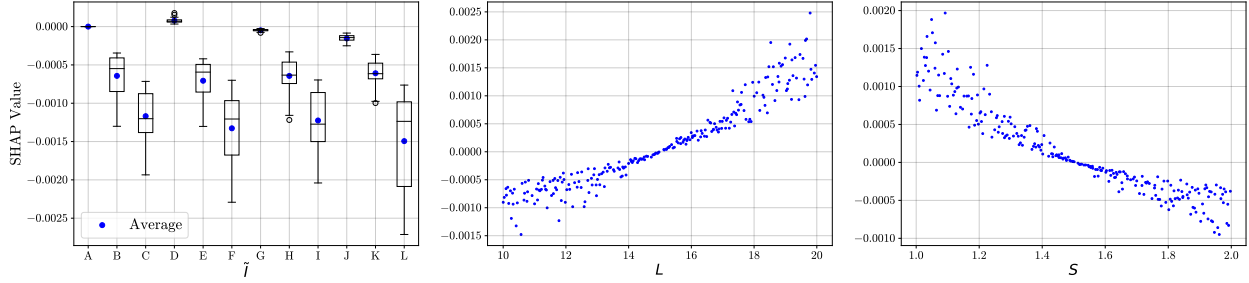


Fig. 11 SHAP dependence plots for the cantilever beam bending problem.

Finally, the feature importance plots are shown in Fig. 12. Both metrics agree that the length of the cantilever beam is a significant factor, given the range of continuous inputs and the type of categorical variable. However, SHAP suggests that L and \tilde{I} have roughly equal importance, whereas PDP identifies L as the most important variable, with \tilde{I} and S following as the next most important variables, showing similar levels of importance. Like PDP, the confidence intervals of the 1D models in Fig. 8 seems to indicate similar importance for \tilde{I} and S and a more important L . In other words, both importance metrics do not fully agree on the importance level of input variables. This difference is due to the distinct perspectives of the two metrics, as previously mentioned in the continuous 10-variable wing weight problem. Although there is a difference in feature importance, it is important to emphasize that both SHAP and PDP/ICE accurately capture the actual trend of the problem, as previously discussed through the dependence plots.

This example illustrates that the explainability module in SMT-EX effectively complements the predictive model by providing a tool that helps users understand the impact of continuous and categorical variables.

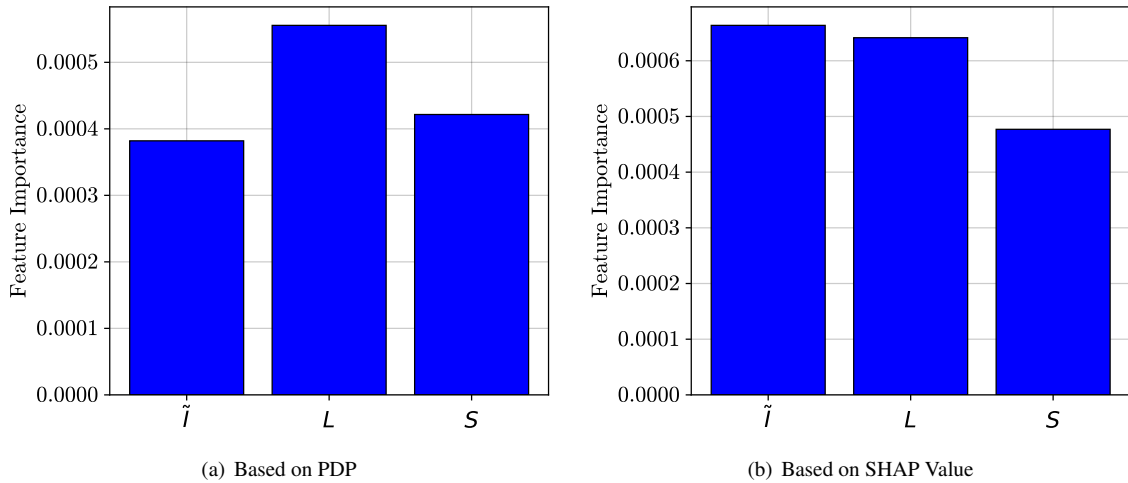


Fig. 12 Feature importance of the cantilever beam bending problem.

V. Conclusion

SMT is a flexible Python-based surrogate modelling tool designed to handle a wide range of input problems, including those involving categorical variables. To further enhance its utility, this paper introduces an explainability module for the SMT tool, called SMT-EX. This module enables users to explore the constructed surrogate models, providing valuable insights into their behaviour and predictions. Once the model is built, the explainability module can be easily accessed, enhancing user interaction with the model. Currently, SMT-EX incorporates three explainability methods: SHAP, PDP, and ICE. This enables SMT users to gain deeper insights into the characteristics of the constructed surrogate model, facilitating a thorough understanding of the relationships between input variables and the output. Besides, we have also implemented Sobol’ indices as a “conventional” means for GSA and uncertainty quantification based on conformal prediction. The conformal prediction itself serves as a method to make the method more “transparent”, similar to the

way GP provides the uncertainty estimate. As such, the availability of uncertainty estimates also falls under the umbrella of explainability. Leveraging the capabilities of SMT, our software effectively manages both mixed-categorical and continuous variables. We advocate for a paradigm shift in how engineers perceive their surrogate models—viewing them not merely as predictive tools but as insightful frameworks that reveal underlying relationships. This shift can significantly expand their understanding and prove beneficial for future applications. In this regard, we developed SMT-EX as a tool that can help scientists and engineers toward that end.

We demonstrated the capabilities of SMT-EX on two test problems: a mixed-categorical beam problem and a 10-variable wing weight problem, where all variables are continuous. Initially, we constructed an accurate GPR model, as accuracy is fundamental for providing meaningful explainability. Subsequently, we activated the explainability module, which yielded insights through visualizations and sensitivity values generated by SHAP, PDP, and ICE methods. This validation is essential for confirming the utility of the knowledge produced, and we found that our results align with established engineering insights for two well-known problems in mechanics and aircraft design.

Acknowledgement

The work of Pramudita Satria Palar and Mohammad Daffa Robani was supported by Institut Teknologi Bandung through the International Research Collaboration for New and Renewable Energy Program. The work of Saves Paul and Joseph Morlier is part of the activities of ONERA - ISAE - ENAC joint research group. We thank Rémi Lafage for its constant help and for being the administrator of the SMTorg open-source organization on GitHub. The research presented in this paper has been performed in the framework of the COLOSSUS project (Collaborative System of Systems Exploration of Aviation Products, Services and Business Models) and has received funding from the European Union Horizon Europe program under grant agreement n° 101097120. The authors acknowledge the research project MIMICO funded in France by the Agence Nationale de la Recherche (ANR, French National Research Agency), grant number ANR-24-CE23-0380.

References

- [1] Farhat, C., Lesoinne, M., and Le Tallec, P., “Load and motion transfer algorithms for fluid/structure interaction problems with non-matching discrete interfaces: Momentum and energy conservation, optimal discretization and application to aeroelasticity,” *Computer methods in applied mechanics and engineering*, Vol. 157, No. 1-2, 1998, pp. 95–114.
- [2] Yondo, R., Andrés, E., and Valero, E., “A review on design of experiments and surrogate models in aircraft real-time and many-query aerodynamic analyses,” *Progress in aerospace sciences*, Vol. 96, 2018, pp. 23–61.
- [3] Krige, D. G., “A statistical approach to some basic mine valuation problems on the Witwatersrand,” *Journal of the Southern African Institute of Mining and Metallurgy*, Vol. 52, 1951, pp. 119–139.
- [4] Zuhail, L. R., Faza, G. A., Palar, P. S., and Liem, R., “On dimensionality reduction via partial least squares for Kriging-based reliability analysis with active learning,” *Reliability Engineering & System Safety*, Vol. 215, 2021, p. 107848.
- [5] LeCun, Y., Bengio, Y., and Hinton, G., “Deep learning,” *nature*, Vol. 521, No. 7553, 2015, pp. 436–444.
- [6] He, C., Zhang, Y., Gong, D., and Ji, X., “A review of surrogate-assisted evolutionary algorithms for expensive optimization problems,” *Expert Systems with Applications*, Vol. 217, 2023, p. 119495.
- [7] Deb, K., Roy, P. C., and Hussein, R., “Surrogate modeling approaches for multiobjective optimization: Methods, taxonomy, and results,” *Mathematical and Computational Applications*, Vol. 26, No. 1, 2020, p. 5.
- [8] Cheng, K., Lu, Z., Ling, C., and Zhou, S., “Surrogate-assisted global sensitivity analysis: an overview,” *Structural and Multidisciplinary Optimization*, Vol. 61, 2020, pp. 1187–1213.
- [9] Bouhlel, M. A., Hwang, J. T., Bartoli, N., Lafage, R., Morlier, J., and Martins, J. R., “A Python surrogate modeling framework with derivatives,” *Advances in Engineering Software*, Vol. 135, 2019, p. 102662.
- [10] Saves, P., Lafage, R., Bartoli, N., Diouane, Y., Bussemaker, J., Lefebvre, T., Hwang, J. T., Morlier, J., and Martins, J. R., “SMT 2.0: A Surrogate Modeling Toolbox with a focus on hierarchical and mixed variables Gaussian processes,” *Advances in Engineering Software*, Vol. 188, 2024, p. 103571.
- [11] Eliáš, J., Vořechovský, M., and Sadílek, V., “Periodic version of the minimax distance criterion for Monte Carlo integration,” *Advances in Engineering Software*, Vol. 149, 2020, p. 102900.

- [12] Menz, M., Dubreuil, S., Morio, J., Gogu, C., Bartoli, N., and Chiron, M., “Variance based sensitivity analysis for Monte Carlo and importance sampling reliability assessment with Gaussian processes,” *Structural Safety*, Vol. 93, 2021, p. 102116.
- [13] Saves, P., Diouane, Y., Bartoli, N., Lefebvre, T., and Morlier, J., “A mixed-categorical correlation kernel for Gaussian process,” *Neurocomputing*, Vol. 550, 2023, p. 126472.
- [14] Marelli, S., and Sudret, B., “UQLab: A framework for uncertainty quantification in Matlab,” *Vulnerability, uncertainty, and risk: quantification, mitigation, and management*, American Society of Civil Engineers, 2014, pp. 2554–2563.
- [15] Faraci, A., Beaurepaire, P., and Gayton, N., “Review on python toolboxes for kriging surrogate modelling,” *ESREL*, 2022, pp. 854–861.
- [16] Saves, P., Diouane, Y., Bartoli, N., Lefebvre, T., and Morlier, J., “High-dimensional mixed-categorical Gaussian processes with application to multidisciplinary design optimization for a green aircraft,” *Structural and Multidisciplinary Optimization*, Vol. 67, 2024, p. 81.
- [17] Roscher, R., Bohn, B., Duarte, M. F., and Garcke, J., “Explainable machine learning for scientific insights and discoveries,” *Ieee Access*, Vol. 8, 2020, pp. 42200–42216.
- [18] Belle, V., and Papantonis, I., “Principles and practice of explainable machine learning,” *Frontiers in big Data*, Vol. 4, 2021, p. 688969.
- [19] Linardatos, P., Papastefanopoulos, V., and Kotsiantis, S., “Explainable ai: A review of machine learning interpretability methods,” *Entropy*, Vol. 23, No. 1, 2020, p. 18.
- [20] Lundberg, S. M., and Lee, S.-I., “A unified approach to interpreting model predictions,” *Advances in neural information processing systems*, Vol. 30, 2017.
- [21] Apley, D. W., and Zhu, J., “Visualizing the effects of predictor variables in black box supervised learning models,” *Journal of the Royal Statistical Society Series B: Statistical Methodology*, Vol. 82, No. 4, 2020, pp. 1059–1086.
- [22] Friedman, J. H., “Greedy function approximation: a gradient boosting machine,” *Annals of statistics*, 2001, pp. 1189–1232.
- [23] Goldstein, A., Kapelner, A., Bleich, J., and Pitkin, E., “Peeking inside the black box: Visualizing statistical learning with plots of individual conditional expectation,” *journal of Computational and Graphical Statistics*, Vol. 24, No. 1, 2015, pp. 44–65.
- [24] Rohmer, J., and Foerster, E., “Global sensitivity analysis of large-scale numerical landslide models based on Gaussian-Process meta-modeling,” *Computers & geosciences*, Vol. 37, No. 7, 2011, pp. 917–927.
- [25] Tripathy, R., Billionis, I., and Gonzalez, M., “Gaussian processes with built-in dimensionality reduction: Applications to high-dimensional uncertainty propagation,” *Journal of Computational Physics*, Vol. 321, 2016, pp. 191–223.
- [26] Sobol’, I. M., “Global sensitivity indices for nonlinear mathematical models and their Monte Carlo estimates,” *Mathematics and computers in simulation*, Vol. 55, No. 1-3, 2001, pp. 271–280.
- [27] Razavi, S., Jakeman, A., Saltelli, A., Prieur, C., Iooss, B., Borgonovo, E., Plischke, E., Lo Piano, S., Iwanaga, T., Becker, W., Tarantola, S., Guillaume, J. H., Jakeman, J., Gupta, H., Melillo, N., Rabitti, G., Chabridon, V., Duan, Q., Sun, X., Smith, S., Sheikholeslami, R., Hosseini, N., Asadzadeh, M., Puy, A., Kucherenko, S., and Maier, H. R., “The future of sensitivity analysis: an essential discipline for systems modeling and policy support,” *Environmental Modelling & Software*, Vol. 137, 2021, p. 104954.
- [28] Palar, P. S., Zuhail, L. R., and Shimoyama, K., “Enhancing the explainability of regression-based polynomial chaos expansion by Shapley additive explanations,” *Reliability Engineering & System Safety*, Vol. 232, 2023, p. 109045.
- [29] Palar, P. S., Dwianto, Y. B., Zuhail, L. R., Morlier, J., Shimoyama, K., and Obayashi, S., “Multi-objective design space exploration using explainable surrogate models,” *Structural and Multidisciplinary Optimization*, Vol. 67, No. 3, 2024, pp. 1–24.
- [30] Palar, P. S., Nguyen Van, E., Bartoli, N., and Morlier, J., “Design Exploration of a Distributed Electric Propulsion Aircraft Using Explainable Surrogate Models,” *Journal of Aircraft*, 2024, pp. 1–14.
- [31] Da Veiga, S., “Tutorial on conformal prediction and related methods-ETICS 2024 Research School,” 2024.
- [32] Bouhlel, M. A., Bartoli, N., Otsmane, A., and Morlier, J., “Improving kriging surrogates of high-dimensional design models by Partial Least Squares dimension reduction,” *Structural and Multidisciplinary Optimization*, Vol. 53, 2016, pp. 935–952.

- [33] Hwang, J. T., and Martins, J. R., “A fast-prediction surrogate model for large datasets,” *Aerospace Science and Technology*, Vol. 75, 2018, pp. 74–87.
- [34] Bussemaker, J. H., “SBArchOpt: Surrogate-Based Architecture Optimization,” *Journal of Open Source Software*, Vol. 8, 2023, p. 5564.
- [35] Bartoli, N., Lefebvre, T., Dubreuil, S., Olivanti, R., Priem, R., Bons, N., Martin, J., and Morlier, J., “Adaptive modeling strategy for constrained global optimization with application to aerodynamic wing design,” *Aerospace Science and Technology*, Vol. 90, 2019, pp. 85–102.
- [36] Roustant, O., Padonou, E., Deville, Y., Clément, A., Perrin, G., Giorla, J., and Wynn, H., “Group kernels for Gaussian process metamodels with categorical inputs,” *SIAM/ASA Journal on Uncertainty Quantification*, Vol. 8, No. 2, 2020, pp. 775–806.
- [37] Williams, C. K., and Rasmussen, C. E., *Gaussian processes for machine learning*, MIT press Cambridge, MA, 2006.
- [38] Barber, R. F., Candes, E. J., Ramdas, A., and Tibshirani, R. J., “Conformal prediction beyond exchangeability,” *The Annals of Statistics*, Vol. 51, No. 2, 2023, pp. 816–845.
- [39] Shafer, G., and Vovk, V., “A tutorial on conformal prediction,” *Journal of Machine Learning Research*, Vol. 9, No. 3, 2008.
- [40] Gamboa, F., Janon, A., Klein, T., Lagnoux, A., and Prieur, C., “Statistical inference for Sobol pick-freeze Monte Carlo method,” *Statistics*, Vol. 50, No. 4, 2016, pp. 881–902.
- [41] Chan, K., Saltelli, A., and Tarantola, S., “Sensitivity analysis of model output: variance-based methods make the difference,” *Proceedings of the 29th conference on Winter simulation*, 1997, pp. 261–268.
- [42] Greenwell, B. M., Boehmke, B. C., and McCarthy, A. J., “A simple and effective model-based variable importance measure,” *arXiv preprint arXiv:1805.04755*, 2018.
- [43] Shapley, L. S., “A value for n-person games,” *Contribution to the Theory of Games*, Vol. 2, 1953.
- [44] Covert, I., and Lee, S.-I., “Improving kernelshap: Practical shapley value estimation using linear regression,” *International Conference on Artificial Intelligence and Statistics*, PMLR, 2021, pp. 3457–3465.
- [45] Forrester, A., Sobester, A., and Keane, A., *Engineering design via surrogate modelling: a practical guide*, John Wiley & Sons, 2008.
- [46] Palar, P. S., Zuhail, L. R., Shimoyama, K., Dwianto, Y. B., and Morlier, J., “Shapley additive explanations for knowledge discovery via surrogate models,” *AIAA SCITECH 2023 Forum*, 2023, p. 0332.
- [47] Iooss, B., Vincent, C., and Thouvenot, V., “Variance-based importance measures for machine learning model interpretability,” *23e Congrès de Maîtrise des Risques et de Sécurité de Fonctionnement*, 2022, pp. 1–13.
- [48] Pelamatti, J., Brevault, L., Balesdent, M., Talbi, E.-G., and Guerin, Y., “Efficient global optimization of constrained mixed variable problems,” *Journal of Global Optimization*, Vol. 73, 2019, pp. 583–613.